Total Ionizing Dose Radiation Induced Dark Current Random Telegraph Signal in Pinned Photodiode CMOS Image Sensors

Clémentine Durnez, *Student Member, IEEE,* Vincent Goiffon, *Member, IEEE,* Cédric Virmontois, *Member, IEEE,* Serena Rizzolo, *Member, IEEE,* Alexandre Le Roch, *Student Member, IEEE,* Pierre Magnan, *Member, IEEE,* Philippe Paillet, *Senior Member, IEEE,* Claude Marcandella, and Laurent Rubaldo

***Abstract*—In this work, several studies on Total Ionizing Dose effects on Pinned Photodiode CMOS images sensors are presented. More precisely, the evolution of a parasitic signal called Random Telegraph Signal is analysed through several photodiode designs. It is shown that the population of pixels exhibiting this fluctuation depends on the design variants. This population also increases in a different way with the dose: the effects are not same considering a low or high X-rays irradiation. Moreover, a statistical analysis is realized in order to better caracterize the defects responsible for RTS. It turns out that electric field enhancement signature can appear in some specific cases.**

***Index Terms*—Random Telegraph Signal, Radiation induced phenomenon, CMOS image sensor, Total Ionizing Dose, TID, X-rays, Pinned Photodiode, fluctuation**

I. Introduction

CMOS image sensors (CIS) are widely used in many imaging systems ranging from commercial to scientific applications. Every year, they provide increasingly better performances, especially for very low light levels, reaching photon counting capabilities [1]. However, improving sensitivity tends to strengthen the importance of some existing parasitic mechanisms such as Dark Current Random Telegraph Signal (DC-RTS). This phenomenon is caused by a leakage current coming from pixel photodiodes. It leads to discrete variation of the output pixel dark signal with time (see for example typical signals in Sec. III-D). It has previously been shown [2], that DC-RTS is most likely due to generation centers located in the depletion region of the photodiode. Yet, two main possible types of radiation induced RTS centers have emerged [3]. If the CIS is exposed to displacement damage dose, the created RTS centers are bulk silicon defects in the depleted volume of the photodiode. On the other hand, if the CIS is unirradiated or exposed to ionizing radiation, the observed DC-RTS centers come from the oxide interfaces. These two cases lead to different RTS characteristics.Whereas displacement damage dose induced DC-RTS have been extensively studied (see for example [4], [5] and references therein), very little is known about Total Ionizing Dose (TID) induced Dark Current RTS [3], [6], [7] and interface metastable generation centers in integrated circuits in general [8].

C.Durnez, V.Goiffon, S.Rizzolo, A.Le Roch and P.Magnan are with ISAE-SUPAERO, Université de Toulouse, Image Sensor Research Team, Toulouse,France (e-mail: clementine.durnez@isae.fr).

C.Virmontois is with CNES (Centre National d'Études Spatiales), Toulouse, France.

P.Paillet and C.Marcandella are with CEA-DAM, DIF F91297 Arpajon, France.

L.Rubaldo is with SOFRADIR, Veurey-Voroize, France.

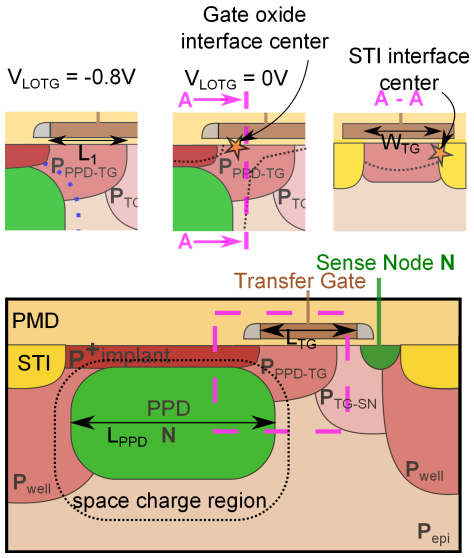

Fig. 1. Cross section of the 4T Pinned Photodiode: L1 represents the zone shared by the P_{PPD-TG} implant and the transfer gate, L_{TG} and W_{TG} are respectively the length and the width of the transfer gate. L_{PPD} is the length of the photodiode.

In the literature, the origin of RTS phenomenon has already been discussed, and it is often attributed to metastable defects exhibiting several possible configurations [9], [10], [11], [5]. The existence of such defects switching spontaneously between several geometrical configurations thanks to the interaction with a phonon has been discussed in several papers [12], [13].

The purpose of this work is to study in details TID induced Dark Current RTS in the main CIS photodetector: the Pinned PhotoDiode (PPD), which is used in more than 99% of CIS today[14]. Especially, this analysis aims at identifying the oxides responsible for this parasitic signal and at

TABLE I
TABLE OF THE STUDIED DESIGNS PARAMETERS

CIS	L_{PPD} (µm)	L_{TG} (µm)	W_{TG} (µm)	L_{I} (µm)
ref	2	0.7	5.27	0.35
#1	4	0.7	5.27	0.35
#2	0.34	0.7	5.27	0.35
#3	2	1.4	5.27	0.35
#4	2	2.1	5.27	0.35
#5	2	0.7	2.63	0.35
#6	2	0.7	1.1	0.35
#7	2	0.7	5.27	0.7

highlighting the influence of design parameters and oxide nature on the observed RTS behavior. To do so, different pixel design variants have been manufactured and analyzed to better locate and understand these metastable generation centers. A statistical study has also been executed in order to underline their different characteristics on amplitudes, time constants and temperature behavior.

II. Experimental details

In order to analyze the influence of many geometrical and physical parameters on RTS centers population, this study uses a set of CIS constituted of 256x256 4T-Pinned Photodiode pixels (which cross section is given in Fig. 1). They are manufactured in a commercially available $0.18\,\mu m$ process, the pixel pitch is $7\,\mu m$, and they are composed of 24 pixel design variants. Two other variations from another CIS (with the same technology, but with different transfer gate shapes) are also used to better support the discussion. Thus the studied devices provide the possibility to analyze the influence of the transfer gate dimensions or the presence of a $P_{PPD\text{-}TG}$ dedicated implant. This latter is a high doped implant to improve charge transfer. For the sake of clarity, only about 10 out of 24 pixel areas of approximately 5000 pixels are examined in this work. They are presented in Tab. I.

Several CIS were irradiated grounded at CEA facility with 10 keV X-ray at total ionizing doses of 300 rad(SiO_2), 3 krad(SiO_2), 10 krad(SiO_2), 50 krad(SiO_2) and 100 krad(SiO_2). The dose rates were 100 rad/s for a total dose below dose below 1krad, and 1 krad/s above. Measurements were done three weeks after irradiation (they were stored at room temperature). Processing was performed thanks to a detection tool which is able to extract RTS pixels automatically with an algorithm based on an edge detection method described in [15]. For each measurement, 5500 images were acquired with an integration time of 1 s at 22°C in dark conditions. 15000 images were also realized in the same conditions from 12°C to 27°C to improve the statistical analysis.

This analysis also focuses on the effects of the transfer gate (TG) low voltage V_{LOTG}. Indeed, during the integration time, a low voltage is applied to the transfer gate so that charges remain stored in the PPD. After this interval of time, they are transferred to the sense node by applying a high voltage (V_{HITG} = 3.3 V) [14]. Thus, as shown in Fig. 1, the low voltage is an important parameter for charge collection and plays a role in the PPD depletion region : a low V_{LOTG} will lessen the space charge region whereas a high V_{LOTG} will widen it. In this last configuration, the photodiode depleted volume reaches oxides and interface states can then participate to the dark current of the PPD. Hence, this configuration allows to scan the oxide interfaces.

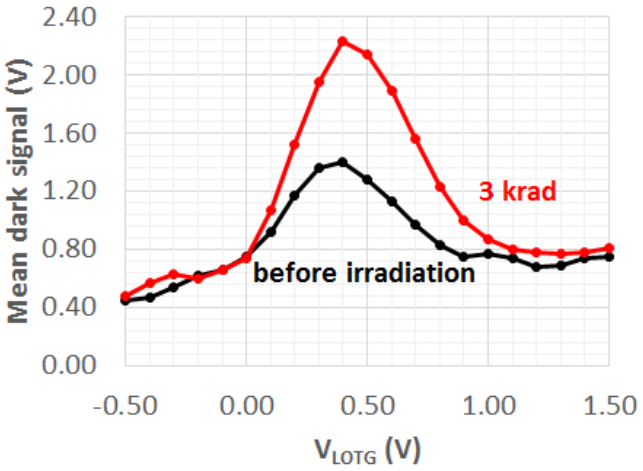

Fig. 2. Mean dark signal measured for several V_{LOTG} before irradiation and after a dose of 3 krad in the reference variant.

III. Experimental Results

A. Mean dark signal behavior

As DC-RTS is extracted in the dark current measurement, the evolution of the mean signal measured on the whole population of reference pixels is shown in Fig. 2. The curves before irradiation and at 3 krad are shown because they correspond to measurements on a same imager. It can be seen that the trends are similar. They also exhibit the same shape than in [16]. Under V_{LOTG} = 0, the collected signal is low. The transfer gate is thus accumulated, and the space charge region is small and does not merge with interfaces. Between 0 V and 0.5 V,the transfer gate is depleted and the space charge region widens, so that it merges with interfaces and the dark signal increases. Above 0.5 V, the generated dark charges leak directly toward the sense node. Thus, they cannot be collected after integration time and the measured dark signal decreases.

Moreover, there is a rise of the mean signal with the irradiation dose, which is due to the increase of the number of defects in the PPD.

Consequently, a variation in the detected RTS pixels ratio depending on V_{LOTG} can be expected, as it is the case for the mean dark signal.

B. Influence of design parameters

In this section, the results before irradiation and after a dose level of 300 rad are similar. That is why, for the sake of visibility, the curves obtained before irradation will not be shown.

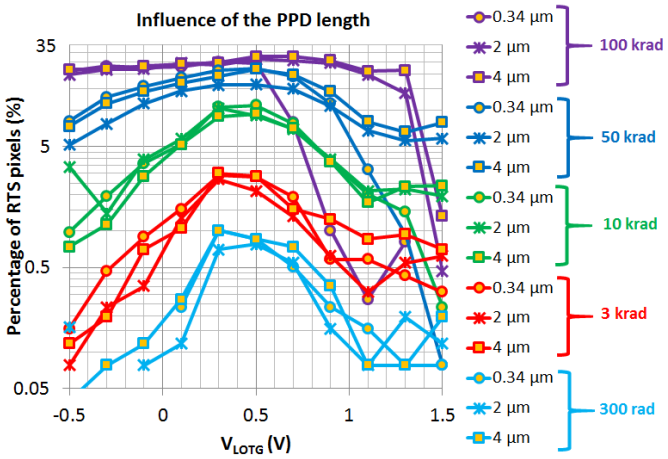

Fig. 3. Ratio of RTS pixels for 3 different photodiode lengths and 5 different TIDs depending on V_{LOTG} (L_{PPD} = 0.34 µm, 2 µm and 4 µm). For the sake of clarity, a semi-logarithmic scale is used. The curves with crosses $*$ correspond to the reference design.

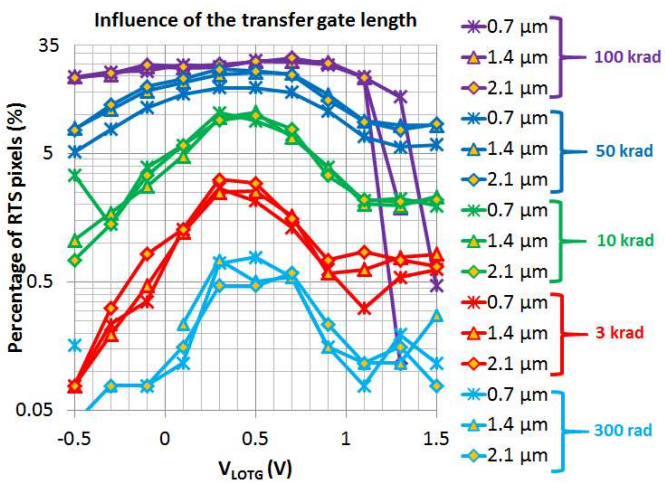

Fig. 4. Ratio of RTS pixels for 3 different transfer gate lengths and 5 different TIDs depending on V_{LOTG} (L_{TG} = 0.7 µm, 1.4 µm and 2.1 µm). The curves with crosses $*$ correspond to the reference design.

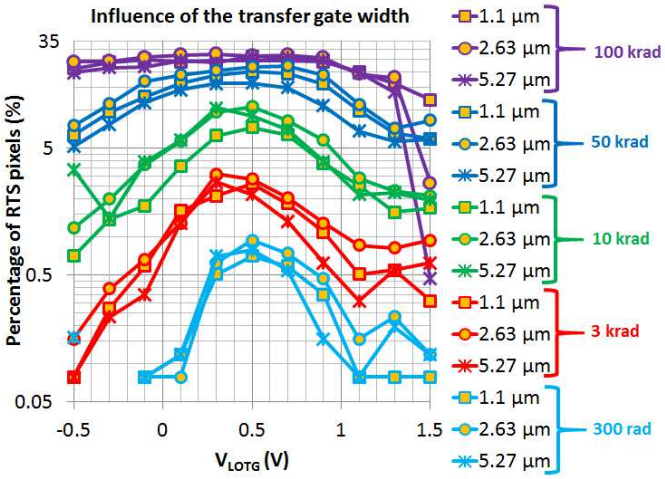

Fig. 5. Ratio of RTS pixels for 3 different transfer gate width and 5 different TIDs depending on V_{LOTG} (W_{TG} = 5.27 µm, 2.63 µm and 1.1 µm). The curves with crosses $*$ correspond to the reference design.

1) Influence of the Photodiode length: Fig. 3 represents the percentage of RTS pixels in 3 distinct pixel variants for 5 TIDs and for several V_{LOTG}. The difference lies in the photodiode length.

First of all, it can be seen that the photodiode length has no influence on the RTS population, because the ratio of RTS pixels remains unchanged between designs for each irradiation dose.

Moreover, for the curves at 300 rad, it is observed that when the transfer gate is accumulated (i.e V_{LOTG}<0), there are almost no RTS pixels. On the contrary, when it is depleted (i.e V_{LOTG}>0), the RTS population increases showing that, at this TID level, all the RTS centers are located at an oxide interface near the TG. In other words, this measurement shows that there is no bulk RTS centers in the studied device. When the transfer gate voltage is higher than 0.7V, the potential below the transfer gate is higher than the potential in the PPD, so that the generated dark charges go directly to the sense node instead of being stored in the photodiode (as detailed in [17]). Hence, the RTS centers have not disappeared but their contribution is no more visible.

Furthermore, the difference between curves from 300 rad to 10 krad is just a translation upward, indicating that the number of RTS centers has increased with the expected TID induced interface state buildup. However, when the ionizing dose increases, the percentage of RTS pixels when the transfer gate is accumulated is no more null. And when the TID level reaches 100 krad, the shape changes completely : DC-RTS behavior is still observed even for negative V_{LOTG}, and the contribution remains constant at positive V_{LOTG} up to at least 1V (except for the smaller length which contribution is hidden by poor performance from 0.5V). This suggests that a new RTS source may be responsible for this phenomenon and that this source is not influenced by V_{LOTG}. For high ionizing doses, a significant amount of positive charges is trapped in the oxides (near the spacer), possibly leading to the depletion of the surface at the PPD/TG edge even for low transfer gate voltages. Thus, RTS centers located in these regions can participate to the dark current at high TID, even when the transfer gate is accumulated.

At high dose (100 krad), it is seen that there are a maximum of about 30% of RTS pixels. However, the contribution of the spacer can be quantified when the transfer gate is accumulated, and is about 20%. It can be deduced that 2/3 of RTS pixels at this dose come from the spacer contribution.

2) Influence of the transfer gate dimensions and bias on DC-RTS: Fig. 4 and Fig. 5 represent the percentage of RTS pixels in 5 distinct pixel variants (3 in each case, but the curve with crosses comes from the same reference design) for 5 TIDs and for several V_{LOTG}. The difference lies respectively in the transfer gate length and width (L_{TG} and W_{TG} in Fig. 1). When the transfer gate length changes, the $P_{PPD\text{-}TG}$ implant remains the same, whereas the $_{TG\text{-}SN}$ implant is extended.

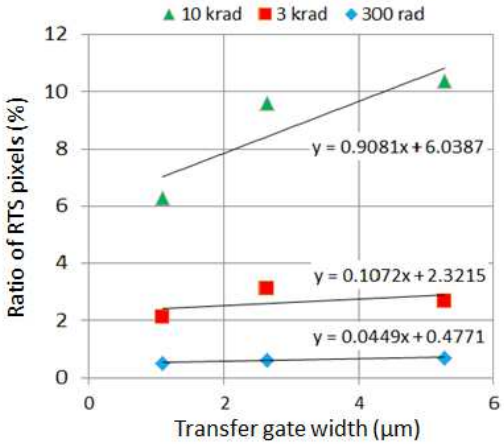

Fig. 6. Ratio of RTS pixels for 3 TIDs depending on the transfer gate width at V_{LOTG} =0.3 V. There seems to be an influence of this parameter.

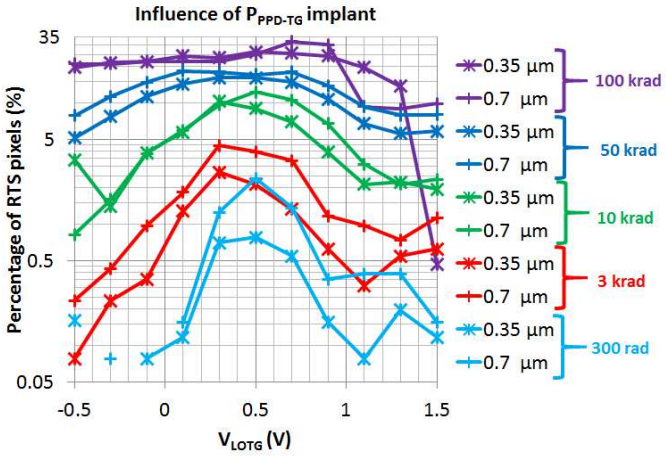

Fig. 7. Ratio of RTS pixels for 2 different P_{PPD-TG} implant lengths and 5 different TIDs depending on V_{LOTG} (L_1 = 0.35 µm and 0.7 µm). The curves with crosses ∗ correspond to the reference design.

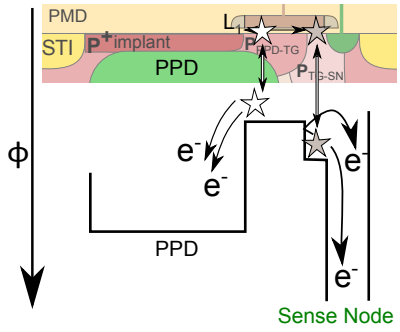

Fig. 8. Potential diagram under the transfer gate, showing a potential step between the photodiode and the sense node.

It can be seen that the transfer gate length does not contribute to RTS phenomenon, because the ratio of RTS pixels remains unchanged between designs for each irradiation dose. This result will be discussed in details in the next section that brings more insight to understand this apparent independence on this parameter.

Fig. 5 shows that there seems to be an influence of transfer gate width between 0 V and 0.5 V, for a low or moderate dose (<50 krad). For example, at V_{LOTG} = 0.3 V, more pixels are detected when the width increases, as shown in Fig. 6. This influence is slight, because for wide transfer gates, the mean dark signal begins to leak at lower V_{LOTG}, and so on, there is a compensation in the phenomenon. The section III-B4 will show more elements to confirm this assessment.

Concerning the shapes of the curves in both Fig. 4 and 5, it can be observed that they exhibit the same behaviour than the previous ones: no RTS when the transfer gate is accumulated at low dose (no bulk RTS centers), but an increase is noticed at high dose (still suggesting an other source induced by TID). The fact that the width has no influence on the RTS pixels ratio (even at high dose) suggests that mostly spacer edges (not the overall spacer along the Transfer Gate) should participate to dark current RTS. Indeed, they are in contact with STI and this implies that they may have more influence than the overall spacer.

3) Influence of the P_{PPD-TG} implant length: Fig. 7 represents the percentage of RTS pixels for 2 distinct areas and 5 TIDs. The design variation is the P_{PPD-TG} implant length on the transfer gate (L_1 in Fig. 1). In the first case (0.35 µm), it corresponds to half of the transfer gate length and then, it covers the entire transfer gate (0.7 µm).

To begin with, the shapes are quite similar to Fig. 3, Fig. 4 and 5: the TID level induces an increase in the percentage of RTS pixels detected. There is just a translation between 300 rad and 10 krad, but there is no more influence of the transfer gate voltage at high dose (100 krad here).

At 300 rad up to 10 krad, it can be observed that when the P_{PPD-TG} implant length is doubled, the ratio of RTS pixels is also doubled, demonstrating that most active centers are located at an oxide interface in the P_{PPD-TG} region. This original result can be explained by the following and is represented on Fig.8: since the doping concentration of the P_{PPD-TG} implant is supposed to be higher than the P doping in the remaining part of the TG channel, the transition from the P_{PPD-TG} region to the P_{TG-SN} region represents a potential step for free electrons. Therefore, any electron originating from a generation center (including RTS ones) in the P_{TG-SN} part of the TG cannot be collected by the photodiode (because of the potential step) and it can only diffuse toward the sense node. On the other hand, dark electrons generated in the P_{PPD-TG} region are free to diffuse toward the PPD or the sense node and thus, the larger is the P_{PPD-TG} region, the higher is the number of active RTS centers.

This mechanism is also the reason why the TG length (L_{TG}) had no influence on the number of RTS pixel in the previous section since only the inactive $_{TG-SN}$ region was extended in the design variation studied in Fig. 4. Despite this first progress, it is not clear whether the STI on the side of the TG channel or the TG oxide itself is contributing to DC-RTS. If the whole TG oxide was the main contributor,

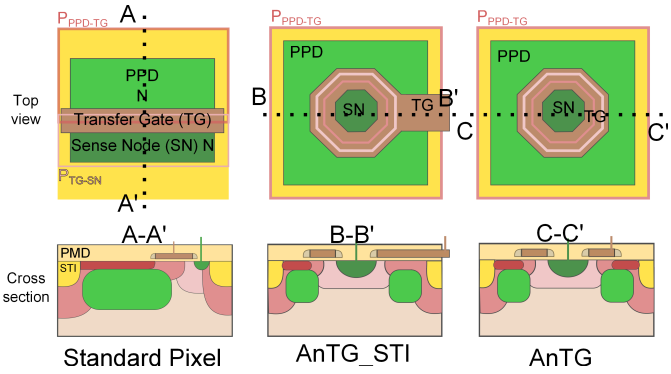

Fig. 9. Top views and Cross sections of a standard pixel and both design variants. The first is called AnTG_STI in opposition to AnTG (which means Annular TG) because it reaches the STI sidewall.

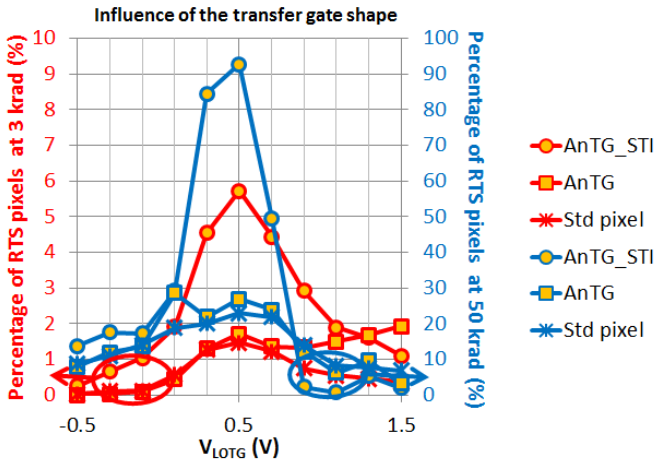

Fig. 10. Ratio of RTS pixels for 3 different transfer gate shapes and 2 different TIDs depending on V_{LOTG}. The primary axis is used for curves at low dose (3 krad), whereas the secondary axis is used for curves at moderate dose.

the number of DC-RTS pixels should rise proportionally to the transfer gate width (whereas no variation is seen in Fig. 5). Hence, the main part of TG channel DC-RTS centers might come from the TG edges or simply from the lateral STI sidewalls (but always in the P_{PPD-TG} region). This assessment will be discussed later in the following part.

Above 10 krad, the curve is more difficult to analyze. As in the previous section III-B2, there are already RTS pixels for negative transfer gate voltages, again suggesting the same new RTS source. This dominating contribution coming from the trapped charge induced depleted interface in the P_{PPD-TG} transition region (i.e. in the TG spacer vicinity) should not be much influenced by P_{PPD-TG} variations.

Moreover, it has been seen that this source is dominating and has nearly the same contribution whatever the value of V_{LOTG} is (at least below 1 V), and the influence of the P_{PPD-TG} implant is no more visible. As previously mentionned for other designs, this indicates that the main source at high ionizing dose is different from the one before irradiation (or at low dose level).

4) Influence of the transfer gate shape: In order to extract STI sidewall (STI on the side of the transfer gate channel) contribution from the spacer vicinity and gate oxide ones and observe their behavior with irradiation, two particular design variants have been used. They are based on an enclosed transfer gate and their cross section are shown in Fig.9. On the one hand, the transfer gate is around the sense node and does not reach any STI sidewall. On the other hand, it is extended to the interface with STI.

Fig. 10 represents the ratio of RTS pixels for the two shapes, for different V_{LOTG} and for two TIDs. It can be observed that for the design AnTG at low dose, almost no RTS pixels are detected when the transfer gate is accumulated. However, some fluctuations appear when the transfer gate is depleted ($V_{LOTG} > 0$). This reinforces the fact the RTS centers cannot be only located on the STI sidewall. The gate oxide also contains defects responsible for this signal. Moreover, at high dose, the influence of the positive charges around the spacer vicinity is observed, because RTS pixels can be seen even when the transfer gate is accumulated.

Concerning the design AnTG_STI, the same conclusion can be drawn when $V_{LOTG} < 0$, but the ratio of RTS pixels when $V_{LOTG} > 0$ is far higher than AnTG.This is explained because first, the gate oxide is larger and also, the interface with STI has an impact too. At moderate dose (50 krad), there is still a peak that remains, showing again the STI sidewall influence when the depletion region is wide enough to reach this interface.

These elements support the fact that when they are unirradiated or with low doses, Pinned PhotoDiodes contain RTS center around the transfer gate (STI sidewall and gate oxide interfaces), because no RTS is observed at negative V_{LOTG}, as seen in [18] (the ratios can be different in that article because unirradiated devices were used and the temperature was not the same). On the other hand, at high dose, RTS fluctuations appear even when the transfer gate is accumulated, showing that trapped charges at the spacer vicinity can play a role. Nevertheless, there is still a contribution of the STI sidewall.

C. Statistical analysis at 10 krad and V_{LOTG} = 0.5V

As irradiation also provides more statistics, it becomes possible to extract relevant RTS parameters. The dose chosen for the analysis is 10 krad.

1) Amplitudes: Fig. 11 shows the histogram of RTS amplitudes for each design containing a P_{PPD-TG} implant in blue (sum of 21 differents PPD schemes). Because the amplitude histogram was found to be similar for each design, it is more relevant to show the sum of all these areas (there are 5703 RTS pixels over 21x5000 pixels). An exponential shape is observed, and the mean amplitude (about 90 e^-/s) is not far from what have been found in the literature [6], [7].

The histogram of the sum of 3 pixel variants is shown in red. It corresponds to photodiodes which do not contain any P_{PPD-TG} implant (there are 1737 RTS pixels over 3x5000 pixels). They have not been studied before because their

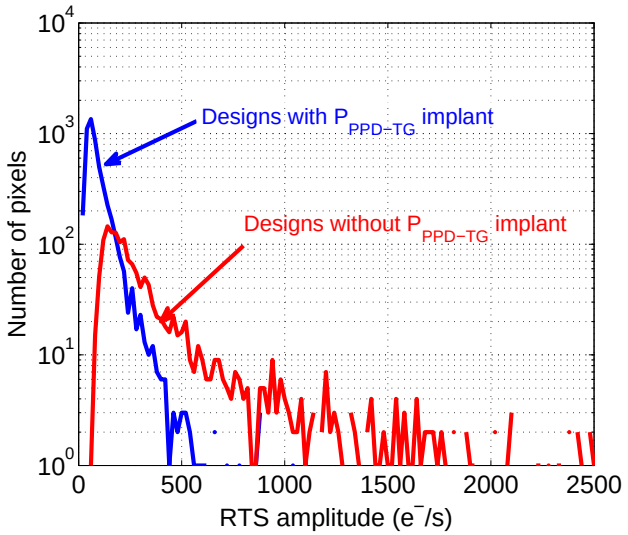

Fig. 11. Histograms of RTS amplitudes for the design variations with $P_{PPD\text{-}TG}$ implant (blue) and for design variations with no $P_{PPD\text{-}TG}$ implant (red).

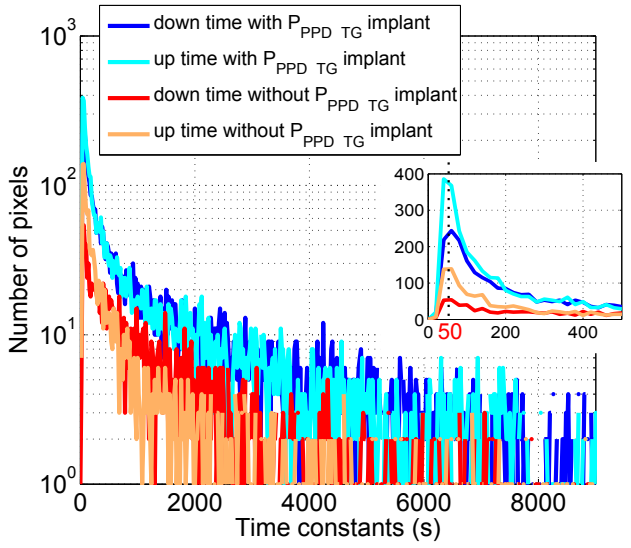

Fig. 12. Histograms of up and down time constants for bi-level RTS for the design variations with $P_{PPD\text{-}TG}$ implant (blue) and for design variations with no $P_{PPD\text{-}TG}$ implant (red). The inset shows a zoom for low time constants.

characteristics are very specific, as it will be analyzed afterwards. But yet, it can already be observed in this Fig. 11 that they have far larger RTS amplitudes, and a high number of RTS pixels. The shape is again exponential, with a mean amplitude of about 400 e-/s.

2) Time constants: Fig.12 represents time constants histograms for bi-level RTS. As the previous section, two design types have been separated : with or without $P_{PPD\text{-}TG}$ doping. On the contrary to what is observed for amplitudes, the same results are found for both types: the same $\frac{A}{x}$ (with A $\approx$ 22000 in the case of the presence of a $P_{PPD\text{-}TG}$ doping) shape and the same peak at τ = 50 s. The translation upward for times with the implant comes from the number of RTS pixels detected.

3) Temperature behavior: This section focuses on designs with $P_{PPD\text{-}TG}$ implant because the next one will be dedicated to the ones with no $P_{PPD\text{-}TG}$ doping. The sum of all these areas containing the implant has been used in order to obtain better results.

The activation energy for amplitude is a key parameter which is often used in the literature [7], [9], [11], [19]. It is calculated as the slope of RTS amplitudes against temperature in semi-logarithmic scale. Indeed, as the generation rate of free carriers is thermally activated, it is possible to extract an exponential mean which corresponds to the activation energy. In dark current studies, if the variation of the defect cross section and the bandgap height are considered as negligible, this activation energy can be related to the defect level in the bandgap of the material, [20]. If the found value is below the mid-gap value, this could suggest particular effects.

Fig.13 shows the different activation energies that have been extracted from the measurements between 12°C and 27°C. The histogram is based on 530 RTS pixels which have been detected for every temperature and with only two

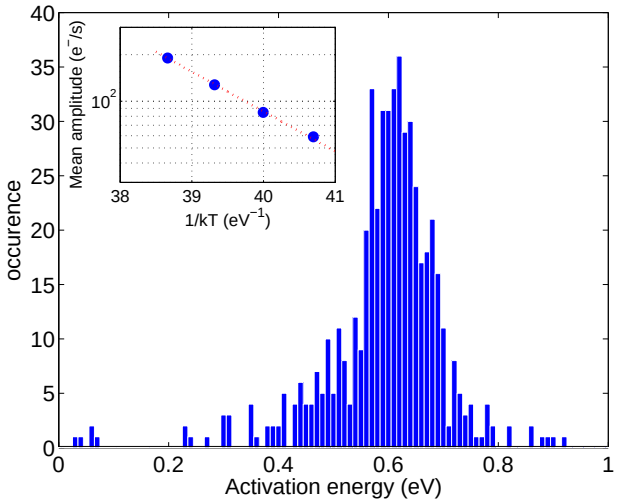

Fig. 13. Histogram of activation energies of amplitudes for RTS centers detected in areas with a $P_{PPD\text{-}TG}$ implant at V_{LOTG} = 0.5 and a total ionizing dose of 10 krad. The activation energies are obtained as shown in the inset on 4 different temperatures between 12°C and 27°C for bi-level RTS.

levels. The mean value is 0.6 $\pm$ 0.1 eV, which is around the mid gap value. It is slightly lower than the one found in [21] in terms of TID, and in agreement with [22]. This strongly suggests a classical Shockley Read Hall phenomenon, on the contrary to what will be seen in the next section.

Concerning time constants, Fig. 14 shows that it is also possible to extract activation energies in the high and low states with Arrhenius plots. The mean found values are 0.73 $\pm$ 0.4 eV in the low state and 0.69 $\pm$ 0.4 eV in the high state).

Some further work should inspect if there is a variation of this activation energy with the TG-OFF voltage V_{LOTG}.

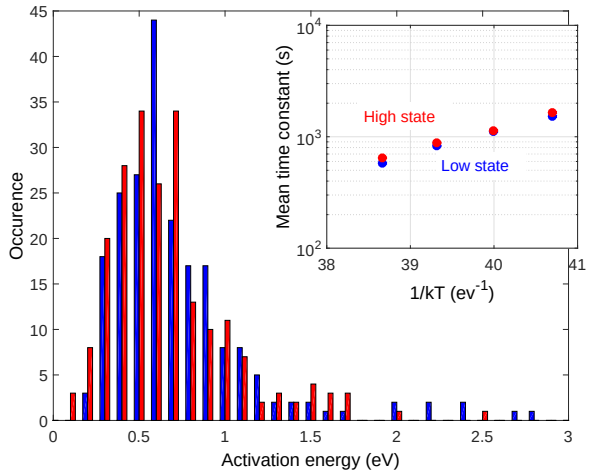

Fig. 14. Histogram of activation energies of time constants for RTS centers detected in areas with a $P_{PPD\text{-}TG}$ implant at V_{LOTG} = 0.5 and a total ionizing dose of 10 krad. The activation energies are obtained as shown in the inset on 4 different temperatures between 12°C and 27°C for bi-level RTS.

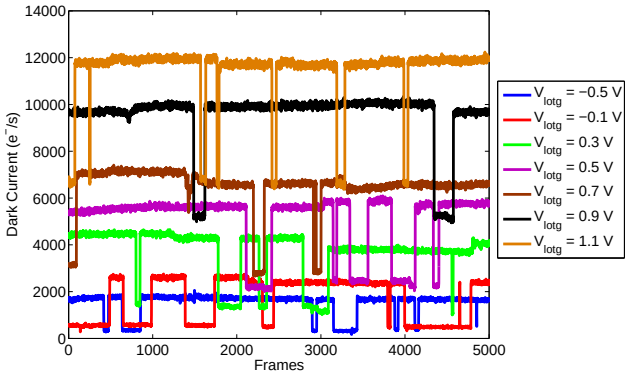

Fig. 15. Evolution of the dark signal of the same RTS pixel with time for different transfer gate voltages at 300 rad.

D. Electric field enhancement (EFE) effect on oxide DC-RTS

Since all DC-RTS centers appear to originate from the $P_{PPD\text{-}TG}$ region of the TG channel (as far as the TID level is not sufficient to deplete the spacer interface), removing this particular implant should have an important effect on radiation induced DC-RTS. This is exactly what was observed on the pixel design without $P_{PPD\text{-}TG}$: there are twice more RTS pixels in average, as explained in Sec.III-C1. In addition to their number, the characteristics of the signal coming from the DC-RTS without this implant are also different. Fig. 15 shows the evolution of such DC-RTS with time at different V_{LOTG}. On the contrary to what is observed in standard designs with the full TG channel doping profile, the amplitude of RTS transition appears to be directly modulated by the TG voltage in the absence of $P_{PPD\text{-}TG}$ implant.

Fig. 16 represents the amplitude variation of the DC-RTS shown in Fig. 15 as a function of V_{LOTG}. The trend is exponential, suggesting an electric field enhancement (EFE)

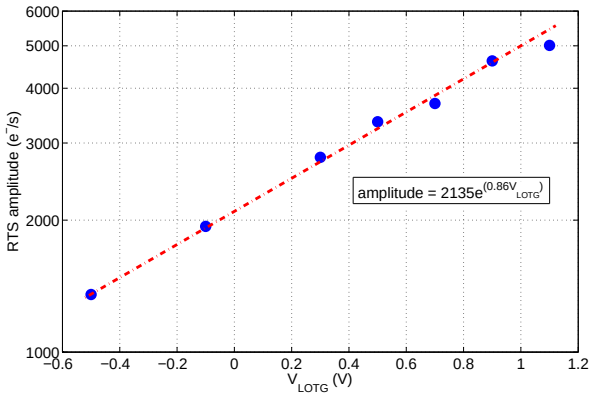

Fig. 16. Evolution of RTS amplitude of a pixel with the transfer gate voltage. On the contrary to usual designs, the amplitude increases exponentially with V_{LOTG}.

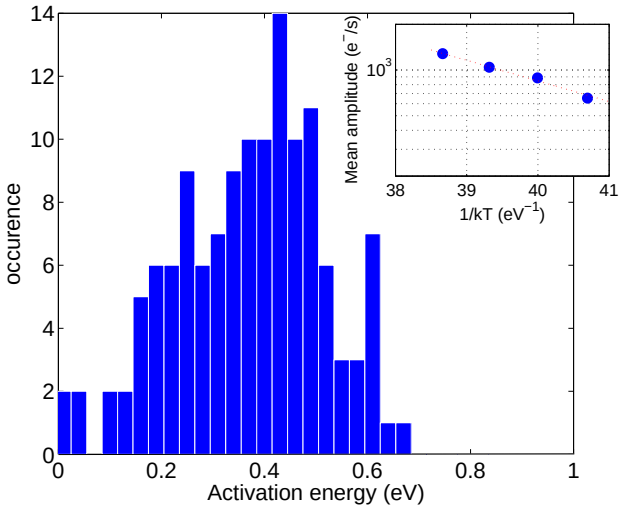

Fig. 17. Histogram of activation energies of amplitudes for RTS centers detected in areas without the $P_{PPD\text{-}TG}$ implant at V_{LOTG} = 0.5 and a total ionizing dose of 10 krad. The activation energies are obtained as shown in the inset on 4 different temperatures between 12°C and 27°C for bi-level RTS.

mechanism [20].

Indeed, if the implant is removed, the substrate, which is less doped, replaces it. This leads to a down shift of the threshold voltage of TG MOSFET in this region, so that the surface potential at the oxide interface is much higher for a given applied voltage than in the case of a nominal TG. This leads to a very high electric field magnitude at the oxide interface.

Another point supporting electric field enhancement is the activation energy of RTS amplitudes in the absence of $P_{PPD\text{-}TG}$ doping. Indeed, it has already been shown that this effect could lower the value for mean dark current [23], [20] and RTS amplitudes [11].

Fig.17 represents the histogram of activation energies found for about 150 bi-level RTS pixels (which have been detected for each temperature measurement) situated in areas with no $P_{PPD\text{-}TG}$ implant. Here, the mean activation energy

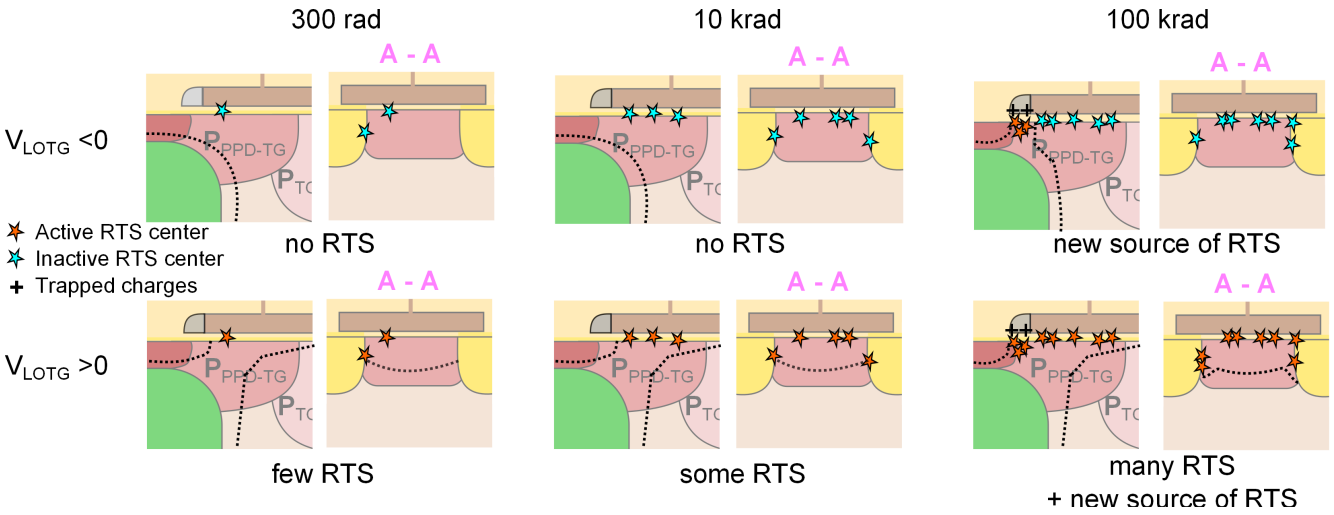

Fig. 18. Possible location for RTS centers. The cross sections are the same than for Fig. 1. At low ionizing dose (300 rad and 10 krad), RTS centers can be situated at oxide interfaces, but for high ionizing dose (100 krad) a new source adds a dark current contribution whatever the transfer gate voltage.

is 0.3 $\pm$ 0.25 eV (the precision is not accurate because of the low number of RTS pixels considered), which is below mid-gap value whereas in standard designs where the electric field is not so high such as the ones studied just before and the literature [21], it is found that this value is around 0.6 eV. Consequently, it can be inferred that electric field enhancement is actually involved in areas with no P_{PPD-TG} implant, reducing the activation energy. Therefore, it seems that the P_{PPD-TG} implant prevents electric field from being high at the oxide interfaces.

Concerning time constants, the activation energies in the high and low states have also been extracted. The mean found values are 0.72 $\pm$ 0.4 eV in the low state and 0.66 $\pm$ 0.4 eV in the high state. These activation energies are similar to those extracted in the previous section, suggesting that electric field enhancement does not influence time constants.

IV. Discussion

Previous sections have shown that variations in the pixel design bring new information about RTS centers location in the pixel. Indeed, for low ionizing dose (from 300 rad to 10 krad), the main source for RTS is the TG channel region near the PPD with the P_{PPD-TG} implant. Two oxide interfaces can play a role in this part of the TG when it is depleted: the gate oxide and STI sidewall. According to the independence on the transfer gate width, the STI contribution seems much stronger than the gate oxide one. However, it is possible to conclude that the gate oxide itself also brings a contribution thanks to the AnTG design.

Fig. 18 sums up possible locations of RTS centers. This cartoon explains the effects observed for each ionizing dose for every studied design variation as far as the correct doping profiles are used. When the transfer gate is accumulated, the depleted volume of the photodiode does not touch any oxide and no DC-RTS is seen, until the ionizing dose induces trapped charges in the oxide in the spacer vicinity. In that case, they create local space charge region and RTS centers can participate to the dark current whatever the transfer gate voltage is. Hence, RTS fluctuations become visible even at negative V_{LOTG} for high ionizing doses.

Similarly, when the transfer gate is depleted, the space charge region of the photodiode is wide enough to access oxide interfaces, and RTS signals at TG channel oxide interfaces (gate oxide and/or STI sidewall) become visible. For high ionizing dose, the depleted spacer source and the STI sidewall are dominating. The spacer source brings the same contribution as for negative V_{LOTG}, but the STI contribution depends on this transfer gate bias. This is why the total ratio of RTS pixels is still higher for positive V_{LOTG}.

This approach explains also why there is no variation of the transfer gate width, because the contribution of the gate oxide is not the main source when the CIS is exposed to ionizing radiations such as X-rays, the STI sidewall is the major one. At high dose, this is explained by the hypothesis of the spacer edges (not the overall spacer) involvment.

Moreover, the statistical analysis has shown that for standard design with small scheme changes, results are similar to the literature: the amplitudes are lower than for displacement damage effects, and activations energies are in agreement with previous studies [6]. However, this article shows that electric field enhancement can be observed in the photodiode if the P_{PPD-TG} implant is removed. This also implies high RTS amplitudes and low activation energies. Consequently, even if this doping region seems to be a key point concerning RTS in unirradiatd devices, it should not be eliminated.

V. Conclusion

This work gives new knowledge regarding the origin of total ionizing dose induced DC-RTS in CMOS active pixel sensors. It has been shown that the length of the P_{PPD-TG} implant has a great influence on RTS phenomenon at moderate TID (<50 krad) but that for higher radiation

dose, the spacer depleted interface provides about 70% of the active DC-RTS centers. Yet, the $P_{PPD\text{-}TG}$ doping should not be removed to mitigate the phenomenon, because this work has also shown for the first time that oxide DC-RTS can exhibit EFE (in non nominal condition). In this case, amplitude can be modulated. This unwanted effect could be used in purpose to further study the effect of high electric field on metastable interface states.

ACKNOWLEDGMENT

The authors would like to thank the ISAE Image Sensor Team for their help, especially Romain Molina for the design of the image sensors, Federico Pace for his help in the data analysis. They would also like to thank CEA-DAM and UCL (Université Catholique de Louvain) for the irradiation opportunities and facilities.

REFERENCES

[1] C. Niclass, C. Favi, T. Kluter, F. Monnier, and E. Charbon, "Single-photon synchronous detection," *IEEE Journal of Solid-State Circuits*, vol. 44, no. 7, pp. 1977–1989, 2009.

[2] I. H. Hopkins and G. R. Hopkinson, "Further measurements of random telegraph signals in proton irradiated CCDs," *IEEE Trans. Nucl. Sci.*, vol. 42, no. 6, pp. 2074–2081, Dec. 1995.

[3] V. Goiffon, P. Magnan, P. Martin-Gonthier, C. Virmontois, and M. Gaillardin, "Evidence of a novel source of random telegraph signal in CMOS image sensors," *IEEE Electron Device Lett.*, vol. 32, no. 6, pp. 773–775, Jun. 2011.

[4] C. Virmontois, V. Goiffon, P. Magnan, S. Girard, C. Inguimbert, S. Petit, G. Rolland, and O. Saint-Pé, "Displacement damage effects due to neutron and proton irradiations on CMOS image sensors manufactured in deep submicron technology," *IEEE Trans. Nucl. Sci.*, vol. 57, no. 6, pp. 3101–3108, Dec. 2010.

[5] C. Durnez, V. Goiffon, C. Virmontois, J.-M. Belloir, P. Magnan, and L. Rubaldo, "In-depth analysis on radiation induced multi-level dark current random telegraph signal in silicon solid state image sensors," *IEEE Transactions on Nuclear Science*, vol. 64, no. 1, pp. 19–26, 2017.

[6] C. Virmontois, V. Goiffon, P. Magnan, O. Saint-Pé, S. Girard, S. Petit, G. Rolland, and A. Bardoux, "Total ionizing dose versus displacement damage dose induced dark current random telegraph signals in CMOS image sensors," *IEEE Trans. Nucl. Sci.*, vol. 58, no. 6, pp. 3085–3094, Dec. 2011.

[7] E. Martin, T. Nuns, C. Virmontois, J. P. David, and O. Gilard, "Proton and-rays irradiation-induced dark current random telegraph signal in a 0.18-CMOS image sensor," *IEEE Trans. Nucl. Sci.*, vol. 60, no. 4, pp. 2503–2510, Aug. 2013.

[8] E. Simoen and C. Claeys, *Random Telegraph Signals in Semiconductor Devices*, ser. 2053-2563. IOP Publishing, 2016. [Online]. Available: http://dx.doi.org/10.1088/978-0-7503-1272-1

[9] I. H. Hopkins and G. R. Hopkinson, "Random telegraph signals from proton-irradiated CCDs," *IEEE Trans. Nucl. Sci.*, vol. 40, no. 6, pp. 1567–1574, Dec. 1993.

[10] D. Pogány, J. A. Chroboczek, and G. Ghibaudo, "Random telegraph signal noise mechanisms in reverse base current of hot carrier-degraded submicron bipolar transistors: Effect of carrier trapping during stress on noise characteristics," *Journal of Applied Physics*, vol. 89, no. 7, pp. 4049–4058, 2001.

[11] J. Bogaerts, B. Dierickx, and R. Mertens, "Random telegraph signals in a radiation-hardened CMOS active pixel sensor," *IEEE Trans. Nucl. Sci.*, vol. 49, no. 1, pp. 249–257, Feb. 2002.

[12] A. Chantre and L. C. Kimerling, "Configurationally multistable defect in silicon," *Applied physics letters*, vol. 48, no. 15, pp. 1000–1002, 1986.

[13] A. Jay, M. Raine, N. Richard, N. Mousseau, V. Goiffon, A. Hémeryck, and P. Magnan, "Simulation of single particle displacement damage in silicon–part ii: Generation and long-time relaxation of damage structure," *IEEE Transactions on Nuclear Science*, vol. 64, no. 1, pp. 141–148, 2017.

[14] E. R. Fossum, D. B. Hondongwa *et al.*, "A review of the pinned photodiode for CCD and CMOS image sensors," *IEEE J. Electron Devices Soc.*, vol. 2, no. 3, pp. 33–43, 2014.

[15] V. Goiffon, G. R. Hopkinson, P. Magnan, F. Bernard, G. Rolland, and O. Saint-Pé, "Multilevel RTS in proton irradiated CMOS image sensors manufactured in a deep submicron technology," *IEEE Trans. Nucl. Sci.*, vol. 56, no. 4, pp. 2132–2141, Aug. 2009.

[16] V. Goiffon, C. Virmontois, P. Magnan, P. Cervantes, S. Place, M. Gaillardin, S. Girard, P. Paillet, M. Estribeau, and P. Martin-Gonthier, "Identification of radiation induced dark current sources in pinned photodiode CMOS image sensors," *IEEE Transactions on Nuclear Science*, vol. 59, no. 4, pp. 918–926, 2012.

[17] V. Goiffon, M. Estribeau, P. Cervantes, R. Molina, M. Gaillardin, and P. Magnan, "Influence of transfer gate design and bias on the radiation hardness of pinned photodiode CMOS image sensors," *IEEE Transactions on Nuclear Science*, vol. 61, no. 6, pp. 3290–3301, 2014.

[18] C. Durnez, V. Goiffon, S. Rizzolo, P. Magnan, C. Virmontois, and L. Rubaldo, "Localization of dark current random telegraph signal sources in pinned photodiode CMOS image sensors," in *2017 International Conference on Noise and Fluctuations (ICNF)*. IEEE, 2017, pp. 131–134.

[19] M. S. Robbins and L. Gomez Rojas, "An assessment of the bias dependence of displacement damage effects and annealing in silicon charge coupled devices," *IEEE Trans. Nucl. Sci.*, vol. 60, no. 6, pp. 4332–4340, Aug. 2013.

[20] J. R. Srour and R. A. Hartmann, "Enhanced displacement damage effectiveness in irradiated silicon devices," *IEEE Transactions on Nuclear Science*, vol. 36, no. 6, pp. 1825–1830, 1989.

[21] V. Goiffon, C. Virmontois, and P. Magnan, "Investigation of dark current random telegraph signal in pinned photodiode CMOS image sensors," in *Electron Devices Meeting (IEDM), 2011 IEEE International*. IEEE, 2011, pp. 8.4.1–8.4.4.

[22] A. S. Grove and D. J. Fitzgerald, "Surface effects on pn junctions: Characteristics of surface space-charge regions under non-equilibrium conditions," *Solid-State Electronics*, vol. 9, no. 8, pp. 783–806, 1966.

[23] G. Vincent, A. Chantre, and D. Bois, "Electric field effect on the thermal emission of traps in semiconductor junctions," *Journal of Applied Physics*, vol. 50, no. 8, pp. 5484–5487, 1979.